



750 nm visible light-driven overall water splitting to H₂ and O₂ over Boron-doped Zn₃As₂ photocatalyst

Mengzhu Jia^{a,b}, Gongxuan Lu^{a,*}

^a State Key Laboratory for Oxo Synthesis and Selective Oxidation Lanzhou Institute of Chemical Physics, Chinese Academy of Sciences, Lanzhou 730000, China

^b University of Chinese Academy of Sciences, Beijing 100049, China

ARTICLE INFO

Keywords:

B-doped Zn₃As₂
Visible driven photocatalytic water splitting
Apparent quantum efficiency

ABSTRACT

Visible and NIR light count about 95% of solar irradiation on the earth, which has not well utilized in photocatalytic overall water splitting (OWS) since the available catalysts under visible-NIR irradiation are either low-effective or unstable. This obstacle may be overcome by the development of a new semiconductor catalyst with well absorption in the visible region and excellent charge transfer properties and photocatalytic activities for OWS. Here, we report a new catalyst B-doped Zn₃As₂ (B-Zn₃As₂) catalyst with well light response up to 750 nm, and achieves a record apparent quantum efficiency (AQE) of 4.09% at 750 nm for photocatalytic OWS without noble metal and sacrificial reagent addition. 14 times higher HER performance than bare Zn₃As₂, excellent light absorption in the visible region, and the excellent separation of photogenerated charges were obtained over B-Zn₃As₂. B-doping on Zn₃As₂ leads to easier H adsorption and desorption and thereafter results in promoted surface dynamics for OWS.

1. Introduction

The global climate change and fossil energy over-consumption may be amended by the renewable hydrogen energy development. Hydrogen is an important secondary energy with the highest energy density, zero carbon emissions characteristics, and the most ideal energy carrier [1–5]. Photocatalytic OWS to H₂ and O₂ evolution driven by solar light is one of the simplest and the easiest scale-up industrial method for hydrogen production potentially in the future [6–10]. Recently, Domen et al. have realized a solar-to-hydrogen efficiency (STH) of 0.76% for OWS over SrTiO₃:Al catalyst under natural sunlight irradiation [11]. But SrTiO₃:Al catalyst can only be photoexcited by UV light, while the UV light only occupy 5% of all solar energy on the earth [12]. Thus, one of the key issues is to develop a photocatalyst with wide optical absorption in the vis-NIR-light region for stable photocatalytic hydrogen evolution (PHE) reaction [13–18].

So far, many active catalysts have been reported related to the extended absorption to wavelength longer than 580 nm, relying on such as element doping, heterojunction construction, upconversion, and so on [17,19–24]. For example, Co-phosphide/PCN single-active-site photocatalyst, synthesized via atomically dispersed CoP sites on the C₃N₄ nanoparticles surface, showed the AQE of 0.35% for OWS at 580

nm [25]. Zhang and coworkers reported a Y₂Ti₂O₅S₂ catalyst with AQE of 0.05% at 600 nm after loading Rh/Cr₂O₃/IrO₂ co-catalyst by significant inhibition of Y₂Ti₂O₅S₂ oxidation via hybridizing S_{3p} orbital with O_{2p} orbital [26]. We also reported a Cu₂ZnSnS₄/CdS/TiO₂ catalyst with a well lattice-matched structure and achieved photocatalytic OWS to hydrogen and oxygen evolution driven by 675 nm visible-light irradiation [27]. Tian and coworkers used a non-metallic plasma BP@g-C₃N₄ photocatalyst and realized an OWS reaction under 730 nm irradiation [28]. We also reported a Pt/Rh/B_{0.25}Ga_{0.75}As/GaAs catalyst, a typical III-V narrow bandgap material, for OWS under 750 nm [29]. Furthermore, Pt/CdS/NaYF₄-Yb³⁺-Er³⁺ was identified to be active for OWS reaction under 980 nm NIR-light irradiation by vis-NIR upconversion of visible light [30].

Zinc Arsenide (Zn₃As₂) is a typical III-V semiconductor with high electronic mobility, quite light absorption in the visible region, and small direct band-gap [31,32]. It has been widely used in photovoltaic, long-wavelength optoelectronic devices, and IR detectors. Shen et al. Reported a Zn₃As₂ photodetector with excellent flexibility and electrical stability [31]. Zn₃As₂ is also an excellent next-generation photoconductive material and a promising building block for flexible nano-optoelectronic devices. For example, Burgess et al. fabricated a Zn₃As₂ single nanostructure photoconductor device, which showed

* Corresponding author.

E-mail address: gxlu@lzb.ac.cn (G. Lu).

<https://doi.org/10.1016/j.apcatb.2023.123045>

Received 10 May 2023; Received in revised form 14 June 2023; Accepted 23 June 2023

Available online 25 June 2023

0926-3373/© 2023 Elsevier B.V. All rights reserved.

good photosensitivity in the near-infrared and visible ranges [32]. It was reported that Boron doping substitution could build an effective inner electric field in semiconductor catalysts, and enhance the photo-generated charge separation and photocatalytic OWS reaction [29], therefore B doping might lead to similar characters in B-Zn₃As₂ photocatalyst. In this article, B-Zn₃As₂ photocatalysts were synthesized by the solid substitution method (SSM), which presented a record-breaking AQE of 4.09% for OWS reaction under 750 nm irradiation. The HER activity of the B-Zn₃As₂ catalyst was 14 times higher compared with bare Zn₃As₂, while the satisfied stability in multi-cycle reactions had been achieved. The theoretical calculation proved that B-Zn₃As₂ resulted in lower E_{Hae} than that bare Zn₃As₂. The B-Zn₃As₂ photocatalyst exhibited improved charge transfer performance. In addition, the B-Zn₃As₂ catalyst also shows activities for OWS under 980 nm and 1064 nm NIR-light irradiation, respectively.

2. Experimental section

2.1. Materials

All chemicals used in this work were purchased commercially and without additional purification. Zinc Arsenide (Zn₃As₂, Alfa Aesar, 99.999%), Sodium Borohydride (NaBH₄, Chengdu Cologne Chemical Reagent Factory, A.R., ≥97.0%), Deuterium substitute water (D₂O, J&K Scientific, 99.9%), heavy-oxygen water (H₂¹⁸O, J&K Scientific, 90.0%). Deionized pure water was used in all PHE reaction runs.

2.2. Preparation of photocatalysts

B-doped Zn₃As₂ (B-Zn₃As₂) was prepared by a solid substitution method (SSM) using NaBH₄ as a B source. The detail process is shown as follows: Zn₃As₂ and NaBH₄ were mixed according to the mass ratio of 1:4, then the reactants were placed in the tube furnace. The samples were put in an oven under setting temperatures (250, 300, 350, and 400 °C respectively) for elemental doping under the protective atmosphere of argon gas. After 6 h of reaction, the reactant mixture was cooled naturally to 25 °C. Then the preliminary product was cleaned, filtered, and dried (vacuum drying oven, 50 °C) to obtain a B-Zn₃As₂ catalyst. The schematic diagram of the B-Zn₃As₂ photocatalyst preparation route is as follows:

2.3. PHE experiments

The PHE tests were carried out in a sealed quartz reactor (182 mL), and the light irradiation area was about 15.9 cm². The xenon lamp (NBeT, HSX-UV 300) was used as a light source equipped with a specific

wavelength bandpass filter. 30 mg of Zn₃As₂ or B-Zn₃As₂ photocatalyst was mixed in 120 mL of deionized in each run. Before irradiation under typical wavelength light, the reactor was treated ultrasonically for 10 min and then bubbled with Ar gas for 40 min. 0.5 mL sample gas was extracted from the reactor every 30 min and analyzed with a gas chromatograph for the determination of formed gas products Fig. 1.

2.4. Catalyst characterizations

X-ray powder diffractometer (XRD) (Smartlab-SE, Rigaku Corporation, Japan) was used for XRD characterization, applied with a Cu K α source, worked at 40 kV, and 30 mA. X-ray photoelectron spectroscopy (XPS) of catalysts was measured in ESCALAB 250Xi (Thermo Fisher Scientific Company, USA), which operated at a monochromatic Al K α source ($h\nu = 1486.6$ eV) and worked at $\sim 10^{-6}$ Pa chamber pressure. The TEM, HRTEM images and the energy dispersive X-ray spectrometer (EDX) data were obtained from the field emission transmission electron microscope (TF-29, FEI Company, USA), equipped with an acceleration voltage of 3 kV.

2.5. The calculation analysis

The plan-wave and PAW wavefunction methods were applied to the pseudopotentials in structure and surface model optimization and energy calculation of the H absorption energy on the surface of photocatalysts. The PBE function in GGA was used for the exchange energy to describe the electron interaction. For comparison of H absorption on the surface of photocatalysts, the self-consistent energy convergence criterion was 2.0×10^{-5} eV/atom, the force convergence criterion was 0.05 eV/Å, the pressure convergence criterion was 0.1 GPa, and the position convergence criterion was 0.002 Å. The H adsorption energy on the surface of photocatalysts was defined according to the following formula (1):

$$E_{Hae} = E_{H/\text{photocatalyst}} - E_H - E_{\text{photocatalyst}} \quad (1)$$

here, $E_{H/\text{photocatalyst}}$ is the base total energy of H on the photocatalyst, E_H is the adsorption H total energy, $E_{\text{photocatalyst}}$ is the base total energy of the photocatalyst.

3. Results and discussion

3.1. Structure and morphology characterization

To study the variation of the crystal phase and structure during the B-Zn₃As₂ preparation process, the typical B-Zn₃As₂ catalysts were characterized by the XRD method. As patterns shown in Fig. 2a, Zn₃As₂

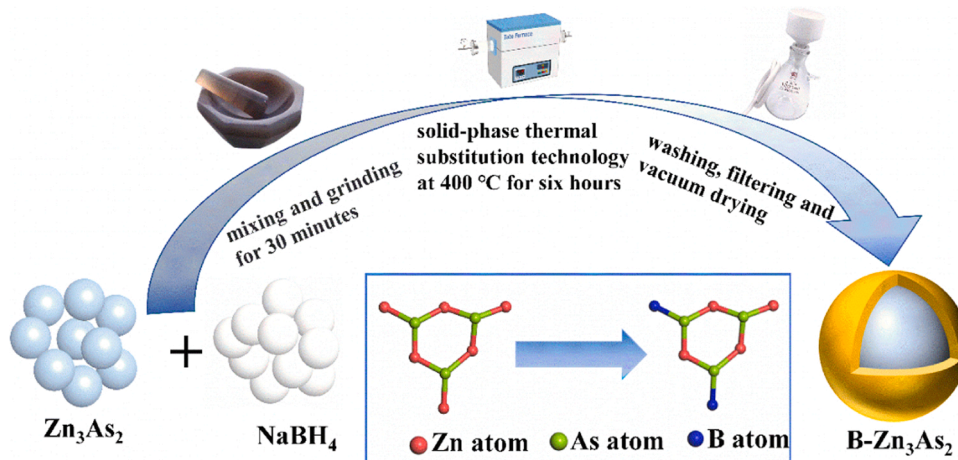


Fig. 1. Schematic diagram of B-Zn₃As₂ photocatalyst preparation.

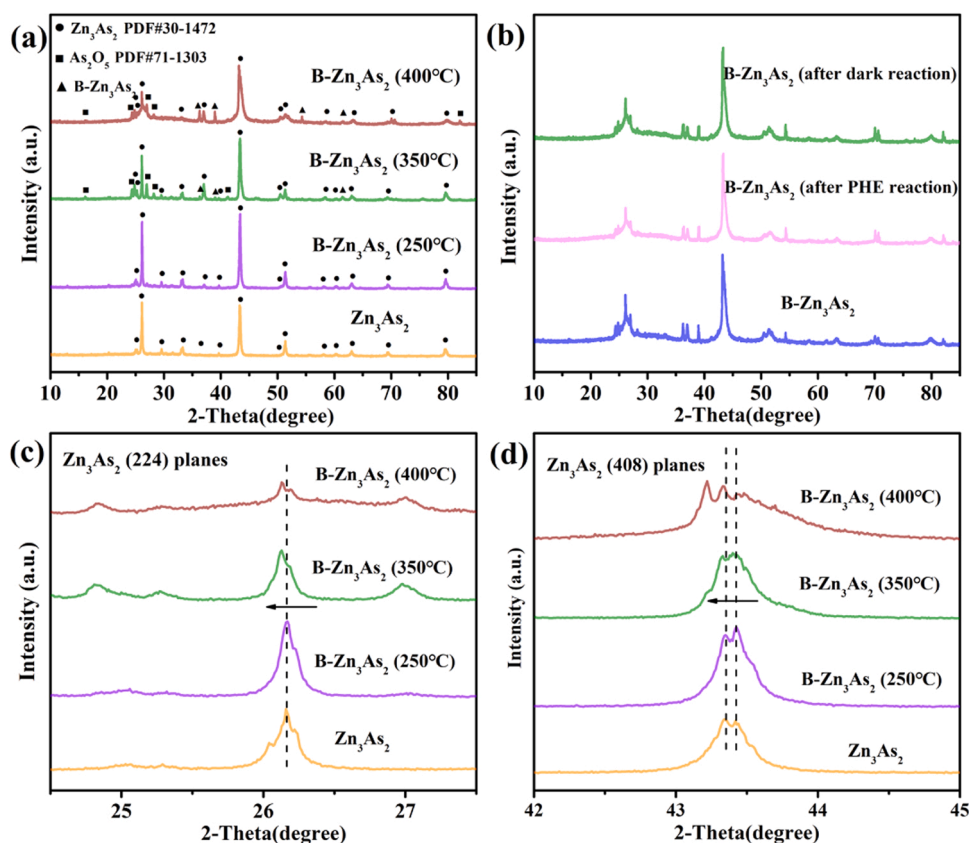


Fig. 2. (a) XRD patterns of photocatalysts, (b) XRD patterns of B-Zn₃As₂ catalysts before and after reaction, (c) the magnified view of Zn₃As₂ (224) planes and (d) the magnified view of Zn₃As₂ (408) planes in B-Zn₃As₂ photocatalysts.

exhibits well crystallinity. The diffraction peaks at 25.0, 26.2, 31.2, 33.1, 38.3, 43.3, 50.7, 51.4, 63.0, 69.3, 79.58° belong to (312), (224), (402), (332), (413), (408), (536), (624), (800), (621), (848) planes of hexagonal crystal phase Zn₃As₂ (PDF 30–1472), respectively [33]. After element substitution doping, the main diffraction peaks belonging to Zn₃As₂ remained, even after the heat treatment in the oven at 400 °C. However, a small amount of Zn₃As₂ was oxidized into As₂O₅ since the weak diffraction peaks appeared at 14.6, 24.1, 28.3, 30.2 and 82.1° which could be attributed to the (110) (111) (201) (211) (711) plane of tetragonal crystal phase As₂O₅ (PDF 71–1303), respectively. Besides, there were some very weak peaks located at 36.3, 39.0, 54.3 and 70.5° in B-Zn₃As₂ catalysts, which represented the B doping products with induced spacing extension in Zn₃As₂. For example, diffraction peaks at 36.3 corresponded to the 2.45 Å lattice spacing in Fig. 3d. In addition, as shown in Fig. 2c and Fig. 2d, the (224) and (408) planes diffraction peaks in B-Zn₃As₂ shifted to a lower diffraction angle weakly, which indicated that the (224) and (408) planes lattice spacing increased, representing the B-atom doping into Zn₃As₂ crystal. According to the XRD of the fresh and the used catalysts in Fig. 2b, the typical diffraction peaks remained unchanged before or after the OWS reaction, indicating the Zn₃As₂ structure was stable during the OWS reaction.

The detailed morphology and surface structure of Zn₃As₂ and B-Zn₃As₂ photocatalysts were also studied by TEM and HRTEM methods. As the TEM images shown in Fig. 3a and Fig. 3b, both Zn₃As₂ and B-Zn₃As₂ photocatalysts give irregular particle morphology with an average size of about 400 nm. HRTEM images in Fig. 3c show the clear (408) and (224) planes of Zn₃As₂ with the typical 2.09 Å and 3.40 Å lattice spacing, respectively. However, the HRTEM image of B-Zn₃As₂ indicated that the (408) plane lattice spacing increased to 2.45 Å, while the (224) plane lattice spacing increased to 3.60 Å, which were consistent with the fact that the (224) and (408) planes of B-Zn₃As₂ shift to a lower angle in the XRD pattern [33], might due to the B-atoms doing

into Zn₃As₂. This conclusion was also supported by the selected electron diffraction pattern of Zn₃As₂ and B-Zn₃As₂ photocatalysts shown in Fig. S1a and Fig. S1b. In that image, the clear core-shell structure in B-Zn₃As₂ photocatalysts can be observed in Fig. S1c and Fig. S1e. The shell thickness can be adjusted by parameters of substitution reaction. The element composition and distribution of the B-Zn₃As₂ photocatalyst were analyzed by EDX and element mapping. As shown in Fig. 3e and Fig. 3f, Zn, As, and B elements can be detected and are well dispersed in the selected region. However, it can be seen clearly that the B element amount is higher in the edge part of the B-Zn₃As₂ photocatalyst particles (yellow elliptic line area in Fig. 3e), demonstrating that the B element content in the edge area is higher than in other areas.

The surface element and chemical state of the Zn₃As₂ and the B-Zn₃As₂ photocatalysts were further analyzed by XPS. XPS survey spectrum shows the clear typical signals of Zn and As elements both in both Zn₃As₂ and B-Zn₃As₂ photocatalysts. As shown in Fig. 4b and Fig. 4c, the Zn 2p spectrum of Zn₃As₂ gave two typical characteristic peaks at 1022.2 eV and 1045.3 eV, corresponding to Zn_{2p3/2} and Zn_{2p1/2} of Zn²⁺ [34]. The Zn Auger kinetic energy spectrum of Zn₃As₂ presented two peaks at 987.1 eV and 990.5 eV, which also indicated that the Zn element was + 2 chemical valence state [34]. For the B-Zn₃As₂, the two characteristic peaks of the Zn binding energy appeared at 1022.1 eV and 1045.1 eV. Similarly, the LMM Auger kinetic energy spectrum of the Zn element appeared at 987.1 eV and 990.1 eV, and kinetic energy moves 0.4 eV. The peak of 40.7 eV in Zn₃As₂ can be attributed to the – 3 valence state of As in Fig. 4d [34], while 44.9 eV belongs to the typical + 3 valence state of As [34]. The two peaks of As in B-Zn₃As₂ appear at 40.4 eV and 44.6 eV, both peaks moved 0.3 eV toward the low binding energy, which might be due to B doping. For the B-Zn₃As₂ photocatalyst, the typical peak of B 1s at 187.7 eV was detected as shown in Fig. 4e, which could be attributed to the B-As bond [29]. The peak at 188.8 eV was the signal of residual NaHB₄ [29]. The peaks at 531.8 eV and

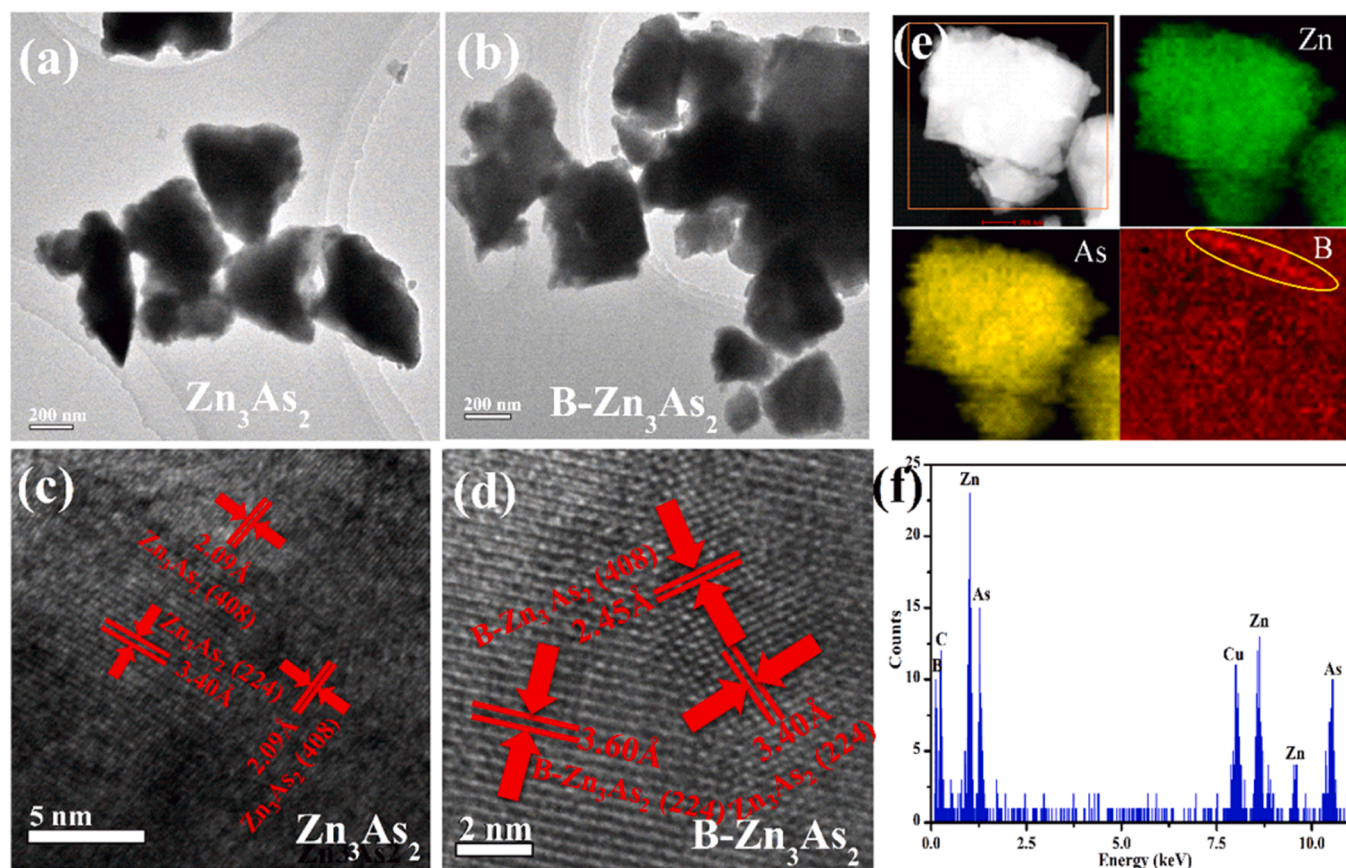


Fig. 3. TEM images of (a) Zn₃As₂ and (b) B-Zn₃As₂ catalysts, HRTEM images of (c) Zn₃As₂ and (d) B-Zn₃As₂, (e) B-Zn₃As₂ elemental mapping images, (f) B-Zn₃As₂ EDX spectrum.

531.7 eV belonged to O1s (shown in Fig. 4f) [34]. A very weak peak at 530.2 eV belonging to the O-Zn bond disappeared in the B-Zn₃As₂ sample [34]. The used B-Zn₃As₂ gave a weak shift in Fig. S2 representing a small amount of As in the B-Zn₃As₂ photocatalyst that was oxidized during the OWS reaction. Nevertheless, Zn 2p, B 1s, and O 1s in the used catalyst did not change, indicating that the B-Zn₃As₂ photocatalyst was stable during the OWS reaction.

3.2. Photocatalytic hydrogen evolution

The OWS activity test was first investigated under light irradiation with the wavelength in the visible region ($\lambda > 420$ nm) without sacrificial reagents addition. According to the results in Fig. 5, the B-Zn₃As₂ photocatalysts exhibited very stable and high activity for OWS. The results in Fig. 5a indicated that the activity for OWS of B-Zn₃As₂ photocatalysts prepared at 400 °C was about 10 times higher than the undoped Zn₃As₂. Increase the substitution doping temperature seems advantageous to the activity promotion of B-Zn₃As₂ for OWS. 400 °C synthesized B-Zn₃As₂ photocatalyst temperatures gave 685.77 $\mu\text{mol}\cdot\text{g}^{-1}$ of hydrogen in 3 h of irradiation, which was about 14 times higher than that of Zn₃As₂. Extending temperature range to higher temperature, for example to 500 °C only gave small increase of PHE activity compared with data of the sample synthesized at 400 °C. The feeding mass ratio of Zn₃As₂ and NaBH₄ affects the B-Zn₃As₂ photocatalyst activity for OWS reaction. The optimized ratio was 1:4. According to results in Fig. S3, the OWS activity of the B-Zn₃As₂ photocatalyst could be optimized by controlling the doping reaction temperature, time, and procedure. In the multi-cycle test, Zn₃As₂ showed a very clear decline tendency and deactivated after two runs in Fig.S4, while the B-Zn₃As₂ photocatalyst remained stable in the eight PHE recycling experiments. The hydrogen evolution remained at 685.77 $\mu\text{mol}\cdot\text{g}^{-1}$ after 8 cycles of experiments

(3 h in each cycle). At the same time, the photo-corrosion resistance properties of the B-Zn₃As₂ photocatalyst were much better than that Zn₃As₂ photocatalyst since the concentration of dissolved As in solution was low in Fig. S5a, indicating that B-Zn₃As₂ has a good photo-corrosion resistance performance and excellent stability.

We also use isotopic tracer experiments using D₂O and H₂¹⁸O as reactants to identify the products in OWS over B-Zn₃As₂ photocatalyst under 750 nm visible-light irradiation [35]. According to the results in Fig. 5c and Fig. 5d, B-Zn₃As₂ can photocatalytic OWS D₂O and H₂¹⁸O into D₂ and ¹⁸O₂ under 750 nm irradiation. Although the ratio of D₂:O₂ and H₂:¹⁸O₂ were not exactly 2:1, the OWS reaction into hydrogen and oxygen was identified because of the different solubility of H₂ and O₂ in water and hydrogen peroxide formation in the OWS reaction (as shown in Fig. S5b).

3.3. Photoelectrical properties

The charge separation and transfer behavior of the B-Zn₃As₂ catalyst were investigated by PL and TRPL methods. As the results in Fig. 6a shown, the PL intensity of B-Zn₃As₂ was lower compared with the Zn₃As₂, which showed that the recombination of photogenerated charge pairs was effectively suppressed by B doping [36]. Furthermore, B-Zn₃As₂ exhibited a much longer lifetime of photoexcited charges than Zn₃As₂ as in Fig. 6b and Table 1. The excited charge lifetime of B-Zn₃As₂ was 12.69 ns, while the lifetime of Zn₃As₂ was only 2.83 ns, the lifetime was remarkably enhanced by B doping and the formation of the electric field built in B-Zn₃As₂ [37]. That conclusion was further supported by electrochemical results. According to LSV results in Fig. 6c, B-Zn₃As₂ exhibited much lower hydrogen production overpotential and higher photocurrent than Zn₃As₂. The onset overpotential for hydrogen formation over the B-Zn₃As₂ catalyst is around -0.78 V, while that over

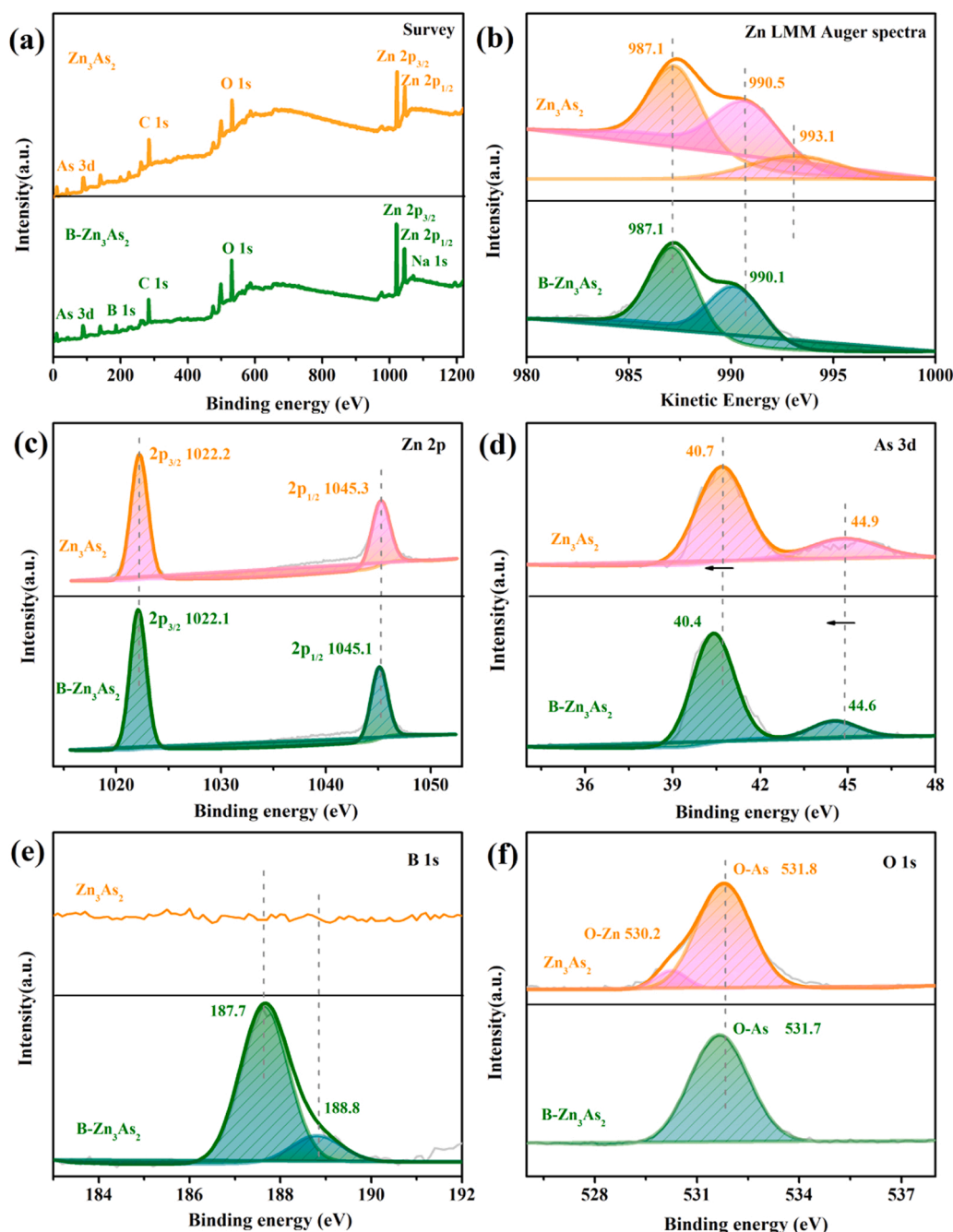


Fig. 4. The XPS spectra of Zn_3As_2 and $\text{B-Zn}_3\text{As}_2$ (a) survey, (b) LMM kinetic energy spectra of Zn element, (c) Zn 2p, (d) As 3d, (e) B 1s, (f) O 1s spectra, respectively.

Zn_3As_2 is about -0.91 V [38]. The $\text{B-Zn}_3\text{As}_2$ catalyst also exhibited higher photocurrent than that of Zn_3As_2 as shown in Fig. S7. $\text{B-Zn}_3\text{As}_2$ presented 5000-ohm resistance, while Zn_3As_2 gave about 26,000-ohm resistance (see EIS results Fig. 6d), demonstrating that B doping significantly enhanced the interfacial charge transport in $\text{B-Zn}_3\text{As}_2$ catalyst [39,40].

3.4. Optical properties and band structures

The absorption properties of the Zn_3As_2 and $\text{B-Zn}_3\text{As}_2$ photocatalysts were investigated by the UV-Vis-NIR DRS method. According to the spectra shown in Fig. 7a, the $\text{B-Zn}_3\text{As}_2$ catalyst can absorb quite a large portion of visible light, even up to the NIR region. The high absorption appeared around 800 nm and B doping could enhance such adsorption between 400 and 100 nm. Although the cutoff edge shifted weakly to the

low wavelength side after B doping, the strong absorption in the visible region remained. The Mott-Schottky plots of Zn_3As_2 and $\text{B-Zn}_3\text{As}_2$ photocatalysts showed that the flat-band positions of the Zn_3As_2 and the $\text{B-Zn}_3\text{As}_2$ were -0.72 and -0.48 V vs. NHE (pH=7), respectively (Fig. S8). Accordingly, the conduction band (CB) of $\text{B-Zn}_3\text{As}_2$ should be lower than that of Zn_3As_2 , which was advantageous for the transfer of photoexcited charges and separation.

The AQE of $\text{B-Zn}_3\text{As}_2$ photocatalyst for OWS was also investigated between 450 nm and 750 nm. As results in Fig. 7b, the AQE variation follows the absorption curve of $\text{B-Zn}_3\text{As}_2$. An AQE of 4.09% has been achieved at 750 nm. According to the data shown in Table S1, this is the highest AQE at 750 nm for OWS reaction compared with the reported values. We also tested the OWS over $\text{B-Zn}_3\text{As}_2$ under 980 nm and 1064 nm irradiation using NIR-light single-photon lasers and found OWS could be realized, the corresponding AQEs were 0.0118% and

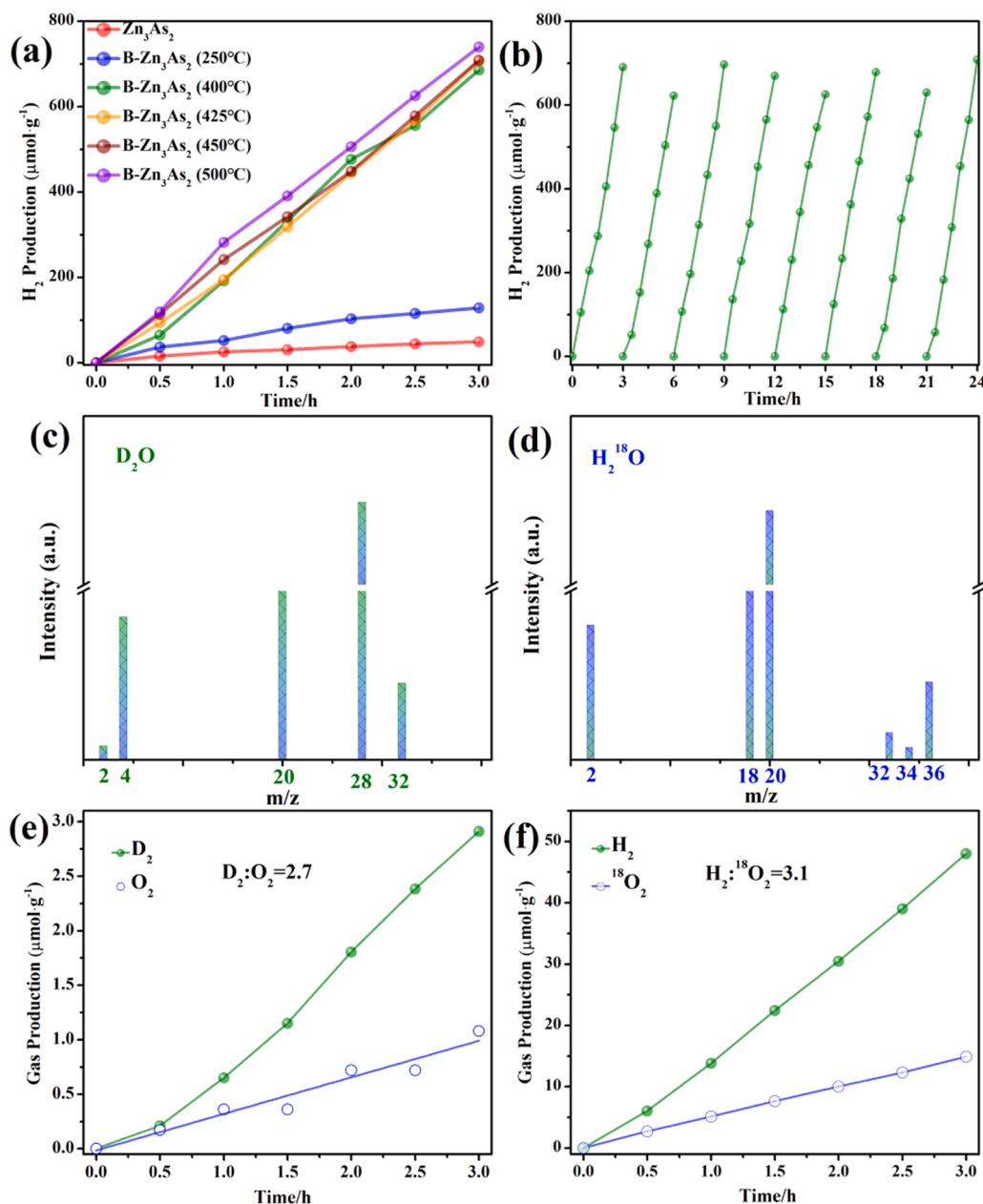


Fig. 5. (a) PHE of Zn₃As₂ and B-Zn₃As₂ photocatalysts, (b) stability test of B-Zn₃As₂ photocatalyst, (c) GC-MS spectra of D₂O isotope label experiment under 750 nm visible-light irradiation, (d) GC-MS spectra of H₂¹⁸O isotope label experiment under 750 nm visible-light irradiation, (e) photocatalytic D₂O splitting over B-Zn₃As₂ photocatalysts, (f) photocatalytic H₂¹⁸O splitting over B-Zn₃As₂ photocatalysts.

0.0054% at 980 nm and 1064 nm (Fig. S9), respectively.

3.5. The hydrogen absorption energy analysis on Zn₃As₂ and B-Zn₃As₂ surface

To analyze the energy relationship between hydrogen absorption and catalyst structure, the H adsorption energies on the typical Zn₃As₂ (224) or B-Zn₃As₂ (224) planes surface were calculated by the DFT method. Several representative H adsorption site models on the Zn₃As₂ (224) plane were carefully investigated, for example, the top sites of As and Zn atoms, the bridge sites between Zn and As atoms, and so on [41, 42]. The top adsorption of 1,2-As site models and 1,2,3,4-Zn site models, the bridge 1,2,3,4,5-Zn-As site models were studied as shown in Fig. 8a and Fig. S10. According to the variation of H adsorption energy at different H adsorption site models on the Zn₃As₂ (224) plane, it is easy to find that the E_{Hae} on the top site of As is always lower than that of the Zn

site, and the lowest E_{Hae} appears on the 2-As top site of the Zn₃As₂ (224) plane, and the corresponding value is -5.88×10^{-22} kJ. And the next lowest E_{Hae} appears on the bridge 4-Zn-As site of the Zn₃As₂ (224) plane with a value of -5.32×10^{-22} kJ, which are the most advantageous sites to H adsorption for OWS on the Zn₃As₂ (224) plane surface. We suppose B substitution may offer several possible sites on B-Zn₃As₂ (224) plane (see Table S2, Fig. S11, Fig. S12 and Fig. S13), and hydrogen is adsorbed on a surface via top adsorption mode on 1,2,3-As sites [29]. The lowest E_{Hae} appears on the 3-As site in the 5-B substituted B-Zn₃As₂ (224) plane, and the corresponding value is -6.06×10^{-22} kJ. It is clear that the E_{Hae} on the B-Zn₃As₂ (224) planes' adsorption site is lower than that of the corresponding Zn₃As₂ (224) plane (see Fig. 6c). Thus, the B-Zn₃As₂ photocatalyst provides a more advantageous H adsorption mode at As-site than Zn₃As₂, which follows the same variation law of OWS activity change over two catalysts [43].

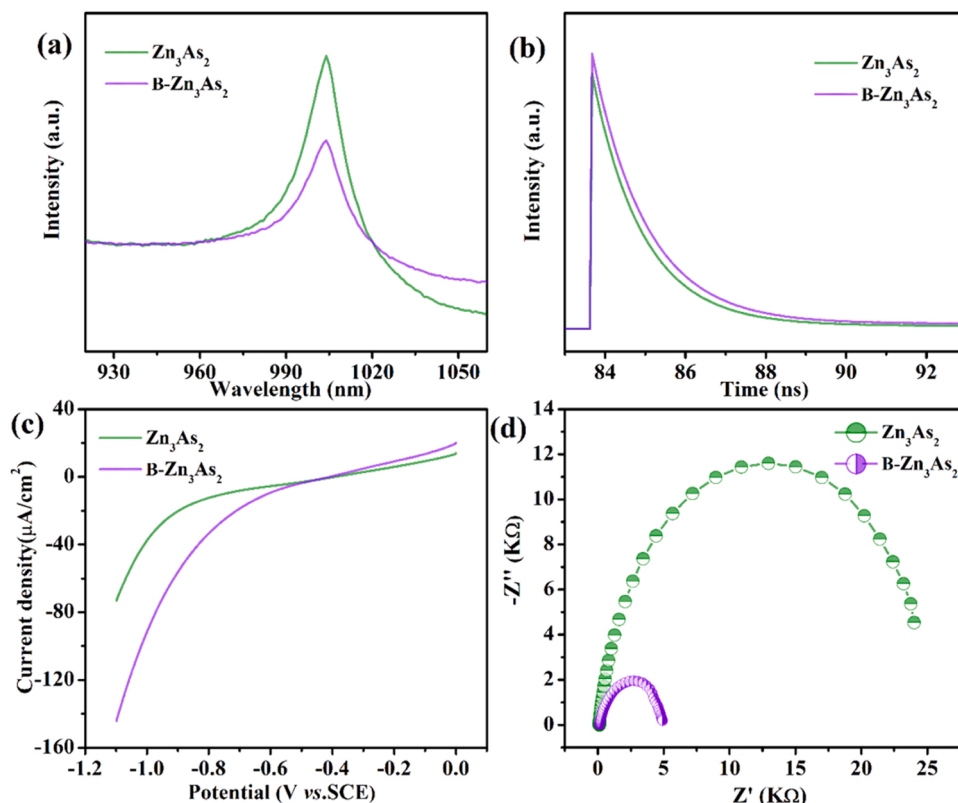


Fig. 6. (a) PL spectra, (b) TRPL decay spectra, (c) LSV curves, (d) EIS of Zn_3As_2 and $\text{B-Zn}_3\text{As}_2$.

Table 1

Summary of the fitted lifetime of Zn_3As_2 and $\text{B-Zn}_3\text{As}_2$ photocatalysts.

sample	τ (ns)	B (%)	Ave. lifetime τ (ns)	χ^2
Zn_3As_2	$\tau_1 = 17.61$	$B_1 = 9.68$	2.83	1.28
	$\tau_2 = 1.25$	$B_2 = 90.32$		
$\text{B-Zn}_3\text{As}_2$	$\tau_1 = 66.03$	$B_1 = 17.54$	12.69	1.25
	$\tau_2 = 1.35$	$B_2 = 82.46$		

Note: τ_1 and τ_2 are the fitted lifetime of photoexcited charges, B_1 and B_2 mean the corresponding proportion. χ^2 represented the residual weighting, and $0.8 < \chi^2 < 1.3$ indicated that the results fitting was reliable and applicable.

4. Conclusion

In this work, $\text{B-Zn}_3\text{As}_2$ photocatalysts synthesized by SSM method are active for OWS reaction and a record AQE of 4.09% for hydrogen generation under 750 nm light irradiation has been achieved. B doping leads to the formation of an effective electric field built in $\text{B-Zn}_3\text{As}_2$

photocatalyst, improved light absorption between 450 nm and 750 nm, enhanced the separation and the transfer of excited charges, presenting about 5 times higher charge lifetime than bare Zn_3As_2 , one-fifth charge transfer resistance of naked Zn_3As_2 and lower hydrogen adsorption energy. $\text{B-Zn}_3\text{As}_2$ catalyst presented 14 times higher activity than bare Zn_3As_2 . B doping on Zn_3As_2 provides an advantageous route for photocatalyst manufacture beneficial for the utilization of longer wavelength solar irradiation on the earth and solar fuel production, such as hydrogen, via photocatalytic OWS reaction.

CRediT authorship contribution statement

Gongxuan Lu conceived and planned the experiments, and Mengzhu Jia performed the related experiments. Gongxuan Lu and Mengzhu Jia wrote and revised the manuscript.

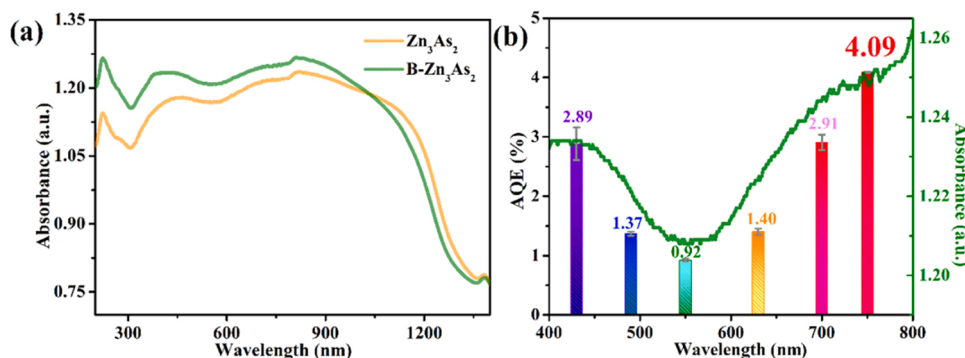


Fig. 7. (a) UV-vis-NIR DRS, (b) AQE of $\text{B-Zn}_3\text{As}_2$ photocatalyst.

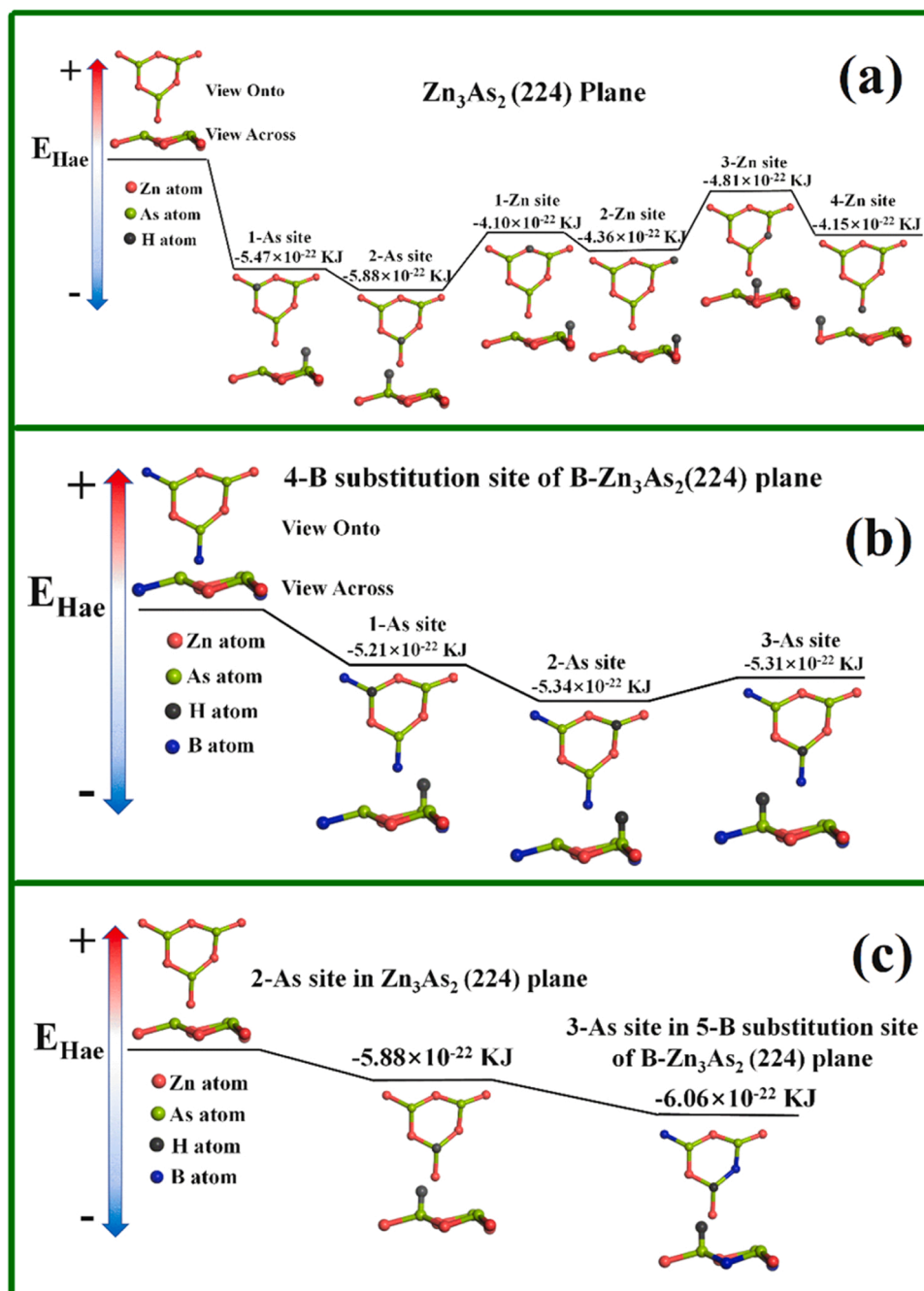


Fig. 8. (a) the top-adsorption sites for H on the Zn_3As_2 (224) plane, (b) the top-adsorption sites for H on the 5-B substitution site of $\text{B-Zn}_3\text{As}_2$ (224) planes, (c) the optimal adsorption sites for H on Zn_3As_2 (224) and $\text{B-Zn}_3\text{As}_2$ (224) plane. The number represents the different sites of Zn, As, and B in Zn_3As_2 (224) and $\text{B-Zn}_3\text{As}_2$ (224) planes, respectively.

Declaration of Competing Interest

The authors declare that they have no known competing financial interests or personal relationships that could have appeared to influence the work reported in this paper.

Data Availability

Data will be made available on request.

Acknowledgement

This work was supported financially by the National Key Research

and Development Program of China (No. 2022YFB3803600), the National Natural Science Foundation of China (22272189 and 22102200), and the Gansu Natural Science Foundation (No. 21JR7RA077 and 22JR5RA105).

Appendix A. Supporting information

Supplementary data associated with this article can be found in the online version at [doi:10.1016/j.apcatb.2023.123045](https://doi.org/10.1016/j.apcatb.2023.123045).

References

- [1] X. Tao, Y. Zhao, S. Wang, C. Li, R. Li, Recent advances and perspectives for solar-driven water splitting using particulate photocatalysts, *Chem. Soc. Rev.* 51 (2022) 3561–3608.
- [2] Z. Wang, C. Li, K. Domen, Recent developments in heterogeneous photocatalysts for solar-driven overall water splitting, *Chem. Soc. Rev.* 48 (2019) 2109–2125.
- [3] Y. Chen, T. Yang, J. Li, M. Wu, J. Shang, Y. Guo, Z. Li, Hydrogen evolution research of Ru-Ni/C catalyst in alkaline medium, *J. Mol. Catal. (China)* 37 (2023) 142–150.
- [4] V. Kumaravel, S. Mathew, J. Bartlett, S.C. Pillai, Photocatalytic hydrogen production using metal doped TiO₂: a review of recent advances, *Appl. Catal. B: Environ.* 244 (2019) 1021–1064.
- [5] W. Gao, W. Zhang, G. Lu, A two-pronged strategy to enhance visible-light-driven overall water splitting via visible-to-ultraviolet upconversion coupling with hydrogen-oxygen recombination inhibition, *Appl. Catal. B: Environ.* 212 (2017) 23–31.
- [6] Q. Wang, K. Domen, Particulate photocatalysts for light-driven water splitting: mechanisms, challenges, and design strategies, *Chem. Rev.* 120 (2020) 919–985.
- [7] S. Chen, T. Takata, K. Domen, Particulate photocatalysts for overall water splitting, *Nat. Rev. Mater.* 2 (2017) 1–17.
- [8] H. Hou, J. Zhang, P. Cai, Y. Lin, Ultrasound-driven deposition of Au nanoparticles on CdS for efficient photocatalytic hydrogen evolution, *J. Mol. Catal. (China)* 36 (2022) 129–136.
- [9] B. Tian, W. Zhen, H. Gao, X. Zhang, Z. Li, G. Lu, Carboxyl-assisted synthesis of Co nanorods with high energy facet on graphene oxide sheets for efficient photocatalytic hydrogen evolution, *Appl. Catal. B: Environ.* 203 (2017) 789–797.
- [10] Z. Li, B. Tian, W. Zhang, X. Zhang, Y. Wu, G. Lu, Enhancing photoactivity for hydrogen generation by electron tunneling via flip-flop hopping over iodinated graphitic carbon nitride, *Appl. Catal. B: Environ.* 204 (2017) 33–42.
- [11] H. Nishiyama, T. Yamada, M. Nakabayashi, Y. Maehara, M. Yamaguchi, Y. Kuromiya, Y. Nagatsuma, H. Tokudome, S. Akiyama, T. Watanabe, R. Narushima, S. Okunaka, N. Shibata, T. Takata, T. Hisatomi, K. Domen, Photocatalytic solar hydrogen production from water on a 100-m² scale, *Nature* 598 (2021) 304–307.
- [12] T. Takata, J. Jiang, Y. Sakata, M. Nakabayashi, N. Shibata, V. Nandal, K. Seki, T. Hisatomi, K. Domen, Photocatalytic water splitting with a quantum efficiency of almost unity, *Nature* 581 (2020) 411–414.
- [13] S. Chen, J.J.M. Vequizo, Z. Pan, T. Hisatomi, M. Nakabayashi, L. Lin, Z. Wang, K. Kato, A. Yamakata, N. Shibata, T. Takata, T. Yamada, K. Domen, Surface modifications of (ZnSe)_{0.5}(CuGa_{2.5}Se_{4.25})_{0.5} to promote photocatalytic Z-scheme overall water splitting, *J. Am. Chem. Soc.* 143 (2021) 10633–10641.
- [14] M. Wang, G. Lu, Improved light harvesting and efficiency for overall water splitting by embedding TiO₂ transition layer in GaP/Ga₂O₃/Ga₂Se₃ multijunction photocatalyst, *Sol. RRL* 5 (2021) 619–631.
- [15] Y. Kageshima, S. Shiga, T. Ode, F. Takagi, H. Shiiba, M.T. Htay, Y. Hashimoto, K. Teshima, K. Domen, H. Nishikiori, Photocatalytic and photoelectrochemical hydrogen evolution from water over Cu₂Sn₃Ge_{1-x}S₃ Particles, *J. Am. Chem. Soc.* 143 (2021) 5698–5708.
- [16] Y. Lu, Y. Li, Y. Wang, J. Zhang, Two-photon induced NIR active core-shell structured WO₃/CdS for enhanced solar light photocatalytic performance, *Appl. Catal. B: Environ.* 272 (2020), 118979.
- [17] W. Gao, Y. Wu, G. Lu, 980 nm NIR light driven overall water splitting over a combined CdS-RGO-NaYF₄-Yb³⁺/Er³⁺ photocatalyst, *Catal. Sci. Technol.* 10 (2020) 2389–2397.
- [18] J. Tian, T. Yan, Z. Qiao, L. Wang, W. Li, J. You, B. Huang, Anion-exchange synthesis of Ag₂S/Ag₃PO₄ core/shell composites with enhanced visible and NIR light photocatalytic performance and the photocatalytic mechanisms, *Appl. Catal. B: Environ.* 209 (2017) 566–578.
- [19] W. Lu, D. Wang, L. Guo, Y. Jia, M. Ye, J. Huang, Z. Li, Y. Peng, W. Yuan, X. Chen, Bipolar carrier transfer channels in epitaxial graphene/SiC core-shell heterojunction for efficient photocatalytic hydrogen evolution, *Adv. Mater.* 27 (2015) 7986–7991.
- [20] X. Zhang, T. Liu, F. Zhao, N. Zhang, Y. Wang, In-situ-formed Cd and Ag₂S decorated CdS photocatalyst with boosted charge carrier spatial separation for enhancing UV–vis–NIR photocatalytic hydrogen evolution, *Appl. Catal. B: Environ.* 298 (2021), 120620.
- [21] X. Ning, W. Zhen, X. Zhang, G. Lu, Assembly of ultra-thin NiO layer over Zn_{1-x}Cd_xS for stable visible-light photocatalytic overall water splitting, *ChemSusChem* 12 (2019) 1410–1420.
- [22] H. Li, J. Xiao, J.J.M. Vequizo, T. Hisatomi, M. Nakabayashi, Z. Pan, N. Shibata, A. Yamakata, T. Takata, K. Domen, One-step excitation overall water splitting over a modified Mg-doped BaTaO₂N photocatalyst, *ACS Catal.* 12 (2022) 10179–10185.
- [23] X. Zhang, H. Guo, G. Dong, Y. Zhang, G. Lu, Y. Bi, Homoeostructural Ta₃N₅ nanotube/nanoparticle photoanodes for highly efficient solar-driven water splitting, *Appl. Catal. B: Environ.* 277 (2020), 119217.
- [24] B. Li, F. He, M. Zhang, A. Abdukayum, Modification of metal organic framework materials and their application of photo-catalytic hydrogen evolution, *J. Mol. Catal. (China)* 37 (2023) 94–107.
- [25] W. Liu, L. Cao, W. Cheng, Y. Cao, X. Liu, W. Zhang, X. Mou, L. Jin, X. Zheng, W. Che, Q. Liu, T. Yao, S. Wei, Single-site active cobalt-based photocatalyst with a long carrier lifetime for spontaneous overall water splitting, *Angew. Chem. Int. Ed.* 56 (2017) 9312–9317.
- [26] G. Zhang, X. Wang, Oxy-sulfide semiconductors for photocatalytic overall water splitting with visible light, *Angew. Chem. Int. Ed.* 58 (2019) 15580–15582.
- [27] X. Zhang, G. Lu, Y. Wu, J. Dong, C. Wang, TiO₂ protection layer and well-matched interfaces enhance the stability of Cu₂ZnSnS₄/CdS/TiO₂ for visible light driven water splitting, *Catal. Sci. Technol.* 11 (2021) 5505–5517.
- [28] B. Tian, Y. Wu, G. Lu, Metal-free plasmonic boron phosphide/graphitic carbon nitride with core-shell structure photocatalysts for overall water splitting, *Appl. Catal. B: Environ.* 280 (2021), 119410.
- [29] X. Zhang, G. Lu, X. Ning, C. Wang, Boron substitution enhanced activity of B₃Ga_{1-x}As/GaAs photocatalyst for water splitting, *Appl. Catal. B: Environ.* 300 (2022), 120690.
- [30] W. Gao, B. Tian, W. Zhang, X. Zhang, Y. Wu, G. Lu, NIR light driven catalytic hydrogen generation over semiconductor photocatalyst coupling up-conversion component, *Appl. Catal. B: Environ.* 257 (2019), 117908.
- [31] G. Chen, Z. Liu, B. Liang, G. Yu, Z. Xie, H. Huang, B. Liu, X. Wang, D. Chen, M.-Q. Zhu, G. Shen, Single-crystalline p-type Zn₃As₂ nanowires for field-effect transistors and visible-light photodetectors on rigid and flexible substrates, *Adv. Func. Mater.* 23 (2013) 2681–2690.
- [32] T. Burgess, P. Caroff, Y. Wang, B.H. Badada, H.E. Jackson, L.M. Smith, Y. Guo, H. H. Tan, C. Jagadish, Zn₃As₂ nanowires and nanoplatelets: Highly efficient infrared emission and photodetection by an earth abundant material, *Nano Lett.* 15 (2015) 378–385.
- [33] H.S. Im, K. Park, D.M. Jang, C.S. Jung, J. Park, S.J. Yoo, J.-G. Kim, Zn₃P₂-Zn₃As₂ solid solution nanowires, *Nano Lett.* 15 (2015) 990–997.
- [34] J.F. Moulder, W.F. Stickle, P.E. Sobol, K.D. Bomben, Handbook of x-ray photoelectron spectroscopy: a reference book of standard spectra for identification and interpretation of XPS data, *Chem. Phys. Lett.* 220 (1992) 36–90.
- [35] B. Tian, W. Gao, X. Ning, Y. Wu, G. Lu, Enhancing water splitting activity by protecting hydrogen evolution activity site from poisoning of oxygen species, *Appl. Catal. B: Environ.* 249 (2019) 138–146.
- [36] K. Fan, Z. Jin, G. Wang, H. Yang, D. Liu, H. Hu, G. Lu, Y. Bi, Distinctive organized molecular assemble of MoS₂, MOF and Co₃O₄, for efficient dye-sensitized photocatalytic H₂ evolution, *Catal. Sci. Technol.* 8 (2018) 2352–2363.
- [37] W. Zhen, X. Ning, B. Yang, Y. Wu, Z. Li, G. Lu, The enhancement of CdS photocatalytic activity for water splitting via anti-photocorrosion by coating Ni₂P shell and removing nascent formed oxygen with artificial gill, *Appl. Catal. B: Environ.* 221 (2018) 243–257.
- [38] X. Zhang, D. Luo, W. Zhang, W. Gao, X. Ning, H. Liu, B. Tian, B. Yang, G. Lu, Inhibition of hydrogen and oxygen recombination over amide-functionalized graphene and the enhancement of photocatalytic hydrogen generation in dye-sensitized AF-RGO/Pt photocatalyst dispersion, *Appl. Catal. B: Environ.* 232 (2018) 371–383.
- [39] X. Ning, W. Zhen, Y. Wu, G. Lu, Inhibition of CdS photocorrosion by Al₂O₃ shell for highly stable photocatalytic overall water splitting under visible light irradiation, *Appl. Catal. B: Environ.* 226 (2018) 373–383.
- [40] W. Zhang, J. Li, G. Lu, H. Guan, L. Hao, Enantiomer-selective sensing and the light response of chiral molecules coated with a persistent luminescent material, *Chem. Commun.* 55 (2019) 13390–13393.
- [41] H. Liu, M. Wang, J. Ma, G. Lu, Modulation of HCHO, H₂O and H adsorption on AgPd cocatalyst by optimizing of selective exposed facet to enhancing the efficiency of conversion toxic formaldehyde into hydrogen driven by visible light, *J. Catal.* 375 (2019) 493–506.
- [42] H. Liu, M. Wang, X. Zhang, J. Ma, G. Lu, High efficient photocatalytic hydrogen evolution from formaldehyde over sensitized Ag@Ag-Pd alloy catalyst under visible light irradiation, *Appl. Catal. B: Environ.* 237 (2018) 563–573.
- [43] H. Liu, M. Wang, J. Ma, G. Lu, Hydrogen generation from toxic formaldehyde catalyzed by low-cost Pd-Sn alloys driven by visible light, *J. Mater. Chem. A* 8 (2020) 9616–9628.